4. J. P. Watt, G. F. Davies, R. J. O'Connell, *Rev. Geophys. Space Phys.* **14**, 541 (1976); R. J. O'Connell and B. Budiansky, *J. Geophys. Res.* **82**, 5719 (1977).
5. H. Kanamori, *J. Geophys. Res.* **72**, 559 (1967); J. Schlittenhardt, *J. Geophys.* **60**, 1 (1986); J. E. Vidale and H. M. Benz, *Nature* **359**, 627 (1993).
6. F. Krüger, M. Weber, F. Scherbaum, J. Schlittenhardt, *Geophys. Res. Lett.* **20**, 1475 (1993); *Geophys. J. Int.* **122**, 637 (1995); F. Krügër, F. Scherbaum, M. Weber, J. Schlittenhardt, *Bull. Seismol. Soc. Am.* **86**, 737 (1996); F. Scherbaum, F. Krüger, M. Weber, *J. Geophys. Res.* **102**, 507 (1997).
7. Traditional stacking assumes that travel-time variation across the array is a linear function of the great-circle distance from the source. This is valid for small aperture arrays and teleseismic data but limits stacking to a single source or sources that are essentially co-located. Double-beam stacking (*6*) relaxes the latter restriction, stacking over receiver and source arrays and resulting in improved slowness and azimuth resolution. The source array aperture, however, must be small in comparison with epicentral distance. With an assumption of a target phase, we can use our approach to stack over large arrays.
8. B. L. N. Kennett, in *International Association of Seismology and Physics of the Earth's Interior (IASPEI) 1991 Seismological Tables*, B. L. N. Kennett, Ed. (Research School of Earth Sciences, Australian National University, Canberra, Australia, 1991), pp. 164–167. We modified the model by depressing the CMB 100 km while retaining the lowermost mantle velocity gradients. This allowed us to compute *PcP* and *PdP* times appropriate for a slow D″ velocity layer without having to alter the overlying velocity structure (for example, slow *PcP* would map as a reflector below the nominal CMB). Ellipticity corrections were applied to the predicted *P* and *PdP* times, the latter approximated by the tabulated correction for *PcP*. Because our focus was on the lowermost mantle, the error in this approximation was ≤0.01 s.
9. Stacking was preceded by alignment of *P* wave forms and deconvolution of the source-time function. Alignment of *P* reduced travel-time variability due to shallow velocity structure and source mislocation. Aligned wave forms were averaged to eliminate variable station-side contributions, leaving the source-time function convolved against a mean mantle response. This was deconvolved from the aligned wave forms, reducing interevent variation of wave form shape to <10% of peak amplitude.
10. To obtain the synthetic stack, we generated ray-theory synthetic data matching the distance distribution of the source region data set and consisting of *P* and *PcP*, the only phases occurring in the absence of a lower mantle reflector. The synthetic seismograms were convolved with the mean deconvolved *P* wave form (*9*) before they were stacked.
11. Residual travel-time variability is parameterized as the standard deviation of a zero-mean Gaussian perturbation applied to delay time in the synthetics.
12. Velocities above the reflector were fixed at IASP91 values for the mean discontinuity depth. We obtained the mean plane-layer reflection coefficient by averaging over the ray parameter weighted by the ray-parameter distribution of stacked data.
13. Amplitudes of *PdP* are affected by variations in lowermost mantle attenuation, velocity heterogeneity, and reflector topography. The factor of 2 expansion of the acceptable range of *R* is intended to avoid the introduction of biases from these factors and from approximations inherent to ray theory. We also required that the resulting mean *PcP* reflection coefficient be positive and less than 0.42 (0.33 for SA) after we applied the same perturbations to velocity and density at the CMB. This constraint eliminates models with large compressional to shear velocity variation ratios. The maximum value for each source region is a factor of 3 greater than the largest accepted estimate (Table 1) to allow for unmodeled variations in geometric spreading and possibly severe attenuation within the LVL.
14. Velocity and density vary linearly across the transition. To compute the mean reflection coefficient, we took the magnitude of the complex reflection coefficient at peak frequency and ignored wave form distortion effects.
15. ν_S and ν_P increases produce *PdP* and *PcP* reflection coefficients that are too large. Some Monte Carlo models had reversed-polarity *PdP*. Eliminating these and accepting only those triplets that predict normal-polarity *PdP* do not affect our conclusions.
16. E. Knittle and R. Jeanloz, *Science* **251**, 1438 (1991); F. Goarant, F. Guyot, J. Peyronneau, J.-P. Poirier, *J. Geophys. Res.* **97**, 4477 (1992); R. Jeanloz, in *Relating Geophysical Structures and Processes: The Jeffreys Volume*, K. Aki and R. Dmowska, Eds., vol. 76 of *Geophysical Monograph Series* (American Geophysical Union, Washington, DC, 1993), pp. 121–127.
17. M. E. Wysession, *Nature* **382**, 244 (1996).
18. S. M. Rigden, T. J. Ahrens, E. M. Stolper, *Science* **226**, 1071 (1984).
19. E. Ito, K. Morooka, O. Ujike, T. Katsura, *J. Geophys. Res.* **100**, 5901 (1995).
20. N. H. Sleep, *Geophys. J. R. Astron. Soc.* **95**, 437 (1988).
21. F. D. Stacey and D. E. Loper, *Phys. Earth Planet. Inter.* **33**, 45 (1983); N. H. Sleep, *J. Geophys. Res.* **97**, 20007 (1992).
22. This research was supported by NSF and Lawrence Livermore National Laboratory, Institute of Geophysics and Planetary Physics. This is Institute of Tectonics contribution 308.

3 March 1997; accepted 17 June 1997

Distance-Dependent Electron Transfer in DNA Hairpins

Frederick D. Lewis,* Taifeng Wu, Yifan Zhang,
Robert L. Letsinger, Scott R. Greenfield,
Michael R. Wasielewski

The distance dependence of photoinduced electron transfer in duplex DNA was determined for a family of synthetic DNA hairpins in which a stilbene dicarboxamide forms a bridge connecting two oligonucleotide arms. Investigation of the fluorescence and transient absorption spectra of these hairpins established that no photoinduced electron transfer occurs for a hairpin that has six deoxyadenosine-deoxythymidine base pairs. However, the introduction of a single deoxyguanosine-deoxycytidine base pair resulted in distance-dependent fluorescence quenching and the formation of the stilbene anion radical. Kinetic analysis suggests that duplex DNA is somewhat more effective than proteins as a medium for electron transfer but that it does not function as a molecular wire.

The occurrence of long-range electron transfer (ET) in duplex DNA remains controversial (*1*). Does the π system of stacked base pairs in B-form DNA function as a molecular wire or as an insulator? Barton and co-workers (*2–5*) have reported several lines of evidence in support of efficient long-range ET involving an electronically excited intercalated metal complex and either a second intercalated metal complex or a "natural" electron donor such as guanine or thymine dimer. The observation of efficient fluorescence quenching in systems with randomly intercalated metal complexes (*2*) and a synthetic 15–base pair duplex in which a donor complex was tethered to the 5′ end of one oligomer and an acceptor complex was tethered to the 5′ end of its complement (*3*) was attributed to the occurrence of long-range ET. This interpretation has recently been questioned on both experimental (*6–8*) and theoretical (*9*) grounds. Current commentaries on this controversy have pointed out the need to determine systematically the dependence of the ET rate constant on the distance separating the donor and acceptor in a series of structurally well-defined supramolecular systems in which the ET process can be directly monitored (*1*).

We report here the results of our investigation of the distance dependence of the photoinduced ET in a family of synthetic DNA hairpins in which a stilbenedicarboxamide forms a bridge connecting two oligonucleotide arms. One of our laboratories previously described the synthesis of thermodynamically stable stilbene-containing hairpins with stems consisting of three or more dA-dT or dG-dC base pairs (*10*). Hairpins with dA-dT stems are fluorescent, whereas hairpins with dG-dC stems are nonfluorescent. Photoinduced ET from guanine to the stilbene singlet state provides a plausible but untested mechanism for fluorescence quenching. Because the transient absorption spectra of both the stilbene singlet state (*11*) and its anion radical

---

F. D. Lewis, T. Wu, Y. Zhang, R. L. Letsinger, Department of Chemistry, Northwestern University, Evanston, IL 60208, USA.
S. R. Greenfield, Chemistry Division, Argonne National Laboratory, Argonne, IL 60439, USA.
M. R. Wasielewski, Department of Chemistry, Northwestern University, Evanston, IL 60208, and Chemistry Division, Argonne National Laboratory, Argonne, IL 60439, USA.

*To whom correspondence should be addressed. E-mail: lewis@chem.nwu.edu

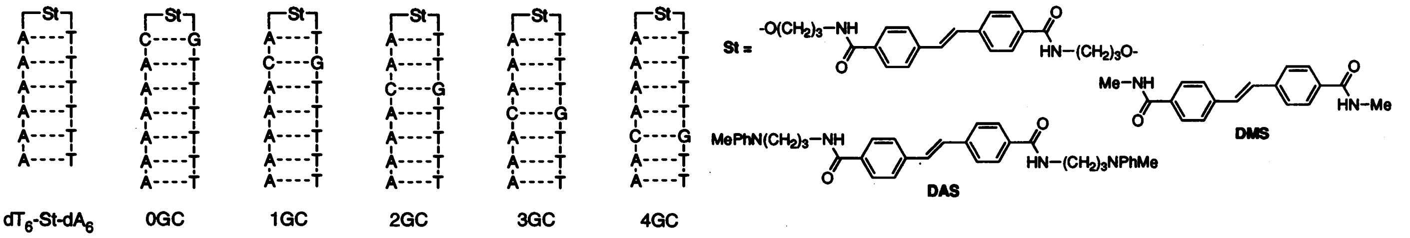

Fig. 1. Formulas of DNA hairpins containing stilbenedicarboxamide bridges and of the model compounds DMS and DAS. Me, methyl.

(*12*) are well characterized and have large extinction coefficients, investigation of ET in these systems is feasible. These observations encouraged us to prepare a family of stilbene-bridged hairpins (Fig. 1) in which the parent hairpin dT_6-St-dA_6 (St, stilbene) is modified by the introduction of a single dG-dC base pair at different positions relative to the stilbene bridge (designated as *n*GC, where *n* is the number of dA-dT base pairs separating the stilbene bridge from the dG-dC base pair). Investigation of the fluorescence and transient absorption spectra of these hairpins establishes that no photoinduced ET occurs for the parent dT_6-St-dA_6. However, introduction of a dG-dC base pair results in distance-dependent fluorescence quenching and the formation of the stilbene anion radical. Kinetic analysis suggests that duplex DNA is somewhat more effective than proteins or saturated hydrocarbons as a medium for ET but that it does not function as a molecular wire.

Molecular modeling of dT_6-St-dA_6 and 0GC to 4GC indicates that they can adopt low-energy conformations in which the base pairs form a B-form double helix with the stilbene located above the adjacent base pair as shown for 4GC in Fig. 2 (*13*). The distance between stilbene and guanine can be readily calculated from either the models or the average π-stacking distance of 3.5 Å. The face-to-face geometry adopted by stilbene and the neighboring base pair is analogous to that proposed for aromatic hydrocarbons in a "dangling" position at the end of a base-paired duplex (*14*).

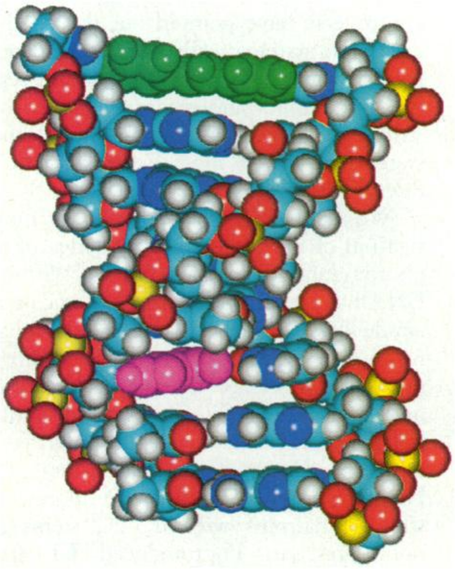

Fig. 2. MM2-minimized structure for the hairpin 4GC. The stilbenedicarboxamide bridge is shown in green at the top of the structure, and the guanine is shown near the bottom of the structure in magenta.

The stilbene-bridged hairpins 0GC to 4GC were synthesized by conventional phosphoramidite chemistry and purified as previously described for dT_6-St-dA_6 (*10*). All of the hairpins displayed two absorption bands with maxima at 334 and 260 nm, the former due exclusively to stilbene and the latter due to the nucleobases and, to a lesser degree, stilbene. Thermal dissociation profiles monitored at 260 nm for the hairpins indicated that they all have melting temperatures >75°C. No hypochromism was observed for the 334-nm stilbene band. Excitation of the hairpins in their long-wavelength absorption band resulted in the observation of fluorescence with maxima at 386 nm, which is characteristic of the stilbenedicarboxamide chromophore (*10*, *15*). Fluorescence quantum yields (Φ_f) for the stilbene-containing hairpins and for the model *N*,*N*-dimethylstilbenedicarboxamide (DMS) are reported in Table 1. The hairpin 0GC is very weakly fluorescent, but the fluorescence intensity increases as the separation between the stilbene chromophore and the dG-dC base pair increases. The fluorescence decay times for dT_6-St-dA_6 and 2GC to 4GC are reported in Table 1 (*16*). Fluorescence decay times for DMS, 0GC, and 1GC are all too short to be measured with our apparatus (<0.3 ns).

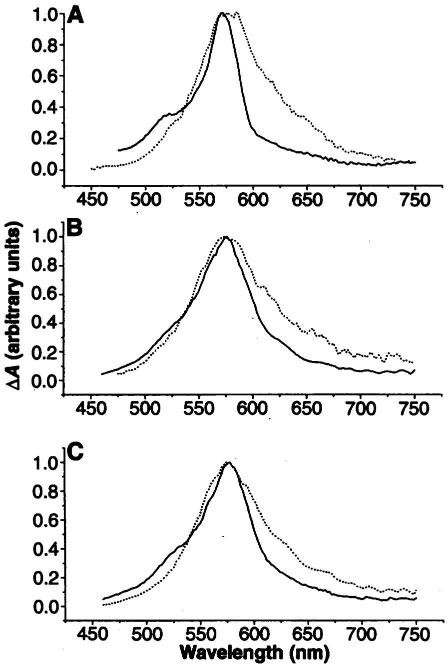

Fig. 3. Transient absorption spectra obtained after a 300-fs excitation at 340 nm; spectra are normalized at their maxima. (**A**) DMS (dashed line) after 2 ps and DAS (solid line) after 10 ps in THF solution. (**B**) dT_6-St-dA_6 (dashed line) after 10 ps and 0GC (solid line) after 2 ps in aqueous solution. (**C**) 2GC after 2 ps (dashed line) and 1 ns (solid line) in aqueous solution. Δ*A* is the change in absorption.

The transient absorption spectra of the stilbene-bridged hairpins were measured with a femtosecond-amplified Ti-sapphire–based laser system that has been described previously (*17*). A ~300-fs, 340-nm laser pulse was used to excite the samples, and a white-light probe pulse of somewhat shorter duration was used to monitor the spectra as a function of time. As models for the stilbenedicarboxamide singlet state and its anion radical, we used DMS and dianilinostilbene (DAS), respectively (Fig. 1). DAS is very weakly fluorescent, in accord with the anticipated occurrence of exergonic intramolecular ET from the tertiary aniline to the stilbene singlet state (*18*). The transient absorption spectra of DMS and DAS obtained at short delay times after 340-nm excitation in tetrahydrofuran (THF) solution are shown in Fig. 3A. These spectra have similar maxima (575 nm), as is commonly the case for the singlet states and anion radicals of planar aromatics. Fortunately, the spectra differ in band shape, that of DMS being broader and having a long-wavelength tail. The 575-nm band of DAS has a short-wavelength shoulder that may obscure the weaker 480-nm absorption band of the tertiary aniline cation radical. In the case of DMS, spectra obtained in

THF, ethanol, and a 1:4 ethanol-water mixture have the same maxima and band shape. The decay of the DMS singlet state (monitored at 575 nm) is singly exponential with a decay time of 42 ps in an ethanol-water mixture, similar to that of the stilbene singlet state in fluid solution (*11*). The formation of the anion radical from the DAS singlet state appears to be complete within 10 ps (Fig. 3A), as is the case for related arene–(trimethylene linker)–aniline systems investigated by Mataga *et al.* (*19*). The decay of the DAS anion radical is singly exponential with a decay time of 730 ps. Substantially slower charge recombination versus charge separation has been observed for related systems and attributed to the much larger energy gap for charge recombination (*19*).

The transient absorption spectra of dT_6-St-dA_6 and 0GC obtained at short decay times (Fig. 3B) resemble those of the model compounds DMS and DAS, respectively (Fig. 3A). The transient absorption spectrum of 0GC does not change with time (2 to 40 ps); however, 1GC to 4GC and dT_6-St-dA_6 display time-dependent transient absorption spectra. The normalized spectra of 2GC (Fig. 3C) resemble that of the stilbene singlet state at short delay times and that of the anion radical at long delay times (Fig. 3A). Similar changes are observed for 1GC and 3GC. Less pronounced changes are observed in the spectra of 4GC and dT_6-St-dA_6, which indicates the persistence of the stilbene singlet at long delay times. The decays of 0GC and 1GC are biexponential, and the shorter and longer decay times are attributed to the decay of the stilbene singlet state and anion radical, respectively. The decays of 2GC to 4GC and dT_6-St-dA_6 are more complex, but decay times for the stilbene singlet can be assigned that are consistent with the fluorescence decay data (Table 1). Anion radical decay times are assigned to the slowest decay components, which in the case of 3GC and 4GC are too slow to measure with our apparatus.

The singlet decay time for dT_6-St-dA_6 is considerably longer than that for the model compound DMS. The decay time of the stilbene singlet state in fluid solution is largely determined by the rate of torsion about the C=C bond, a process that is temperature- and solvent viscosity–dependent (*11*). The long decay time for dT_6-St-dA_6 is consistent with a hairpin structure that restricts C=C torsion (Fig. 2), and, in addition, it indicates that ET quenching of singlet stilbene by neighboring dT-dA base pairs is not an efficient process. In contrast, the extensive quenching of stilbene fluorescence observed for 0GC and the similarity of its transient absorption spectrum to that of the model compound DAS indicate that quenching of singlet stilbene by a neighboring dC-dG base pair occurs through a rapid ET process. The shorter rise and decay times for the anion radical of 0GC versus the model DAS (Table 1) are attributed to the rigid hairpin structure that eliminates the necessity for conformational change before charge separation or recombination.

The difference in behavior of neighboring dC-dG compared with dT-dA base pairs can be attributed to the lower oxidation potential of dG versus dA or the pyrimidine bases dT and dC. Whereas the oxidation potentials (E^0) of the nucleobases have not been directly measured in neutral aqueous solution, recent estimates based on pulse radiolysis data provide values of $E^0 = 1.34$ V for guanosine and 1.79 V for adenosine and greater values for the pyrimidine bases (*20*). The reduction potential of the stilbenedicarboxamide singlet state (*18*) is halfway between these values, thus accounting for the observation of efficient quenching by dG but not for quenching by the other nucleobases. Our failure to detect the cation radical of dG by transient absorption is reasonable because its reported extinction coefficient is lower than those of *N,N*-dialkylanilines (*21*).

Rate constants for photoinduced ET (k_{et}) can be calculated from the measured singlet decay times (Table 1) with the use of

$$k_{et} = \tau_n^{-1} - \tau_0^{-1} \qquad (1)$$

where τ_0 is the decay time for dT_n-St-dA_n and τ_n is the decay time for the *n*GC hairpins. Plotting k_{et} according to

$$k_{et} = Ae^{-\beta R} \qquad (2)$$

where *R* is the distance between the stilbene acceptor and guanine donor, provides Fig. 4. A similar plot is obtained from kinetic analysis of the fluorescence quantum yield data. From the slope of these plots, a value of the distance dependence of the ET rate constant, $\beta = 0.64 \pm 0.1$ Å^{-1}, is obtained. This β value is distinctly greater than that suggested for DNA by the experiments of Barton and co-workers ($\beta < 0.2$ Å^{-1}) (*2*, *3*) but is smaller than the values reported by Brun and Harriman (6) for ET between DNA-intercalated organic donors and acceptors ($\beta \sim 0.9$ Å^{-1}) or for ET in proteins ($\beta = 1.0$ to 1.4 Å^{-1}) (9). The efficiency of ET in our hairpins becomes too small beyond four dA-dT base pairs to permit its detection by fluorescence quenching or transient absorption. However, this result does not preclude inefficient "leakage" over longer distances, which might be responsible for the observation of long-range low-quantum-yield photooxidation of guanine and thymine dimers by Barton and co-workers (*4*, *5*).

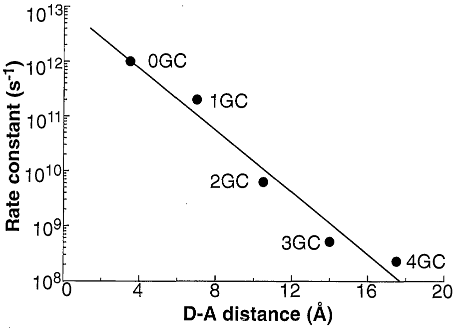

Fig. 4. Donor-acceptor (D-A) distance dependence of the ET rate constant in DNA hairpins containing stilbenedicarboxamide bridges.

Table 1. Fluorescence quantum yields and decay times for St singlets and radical anions. See Fig. 1 for structures. The lack of a decay time value for the DAS singlet indicates that complex short-time kinetics presumably result from multiple ground-state conformations. Dashes indicate that no anion radical is formed.

Compound	Φ_f*	Decay time (ns)	
		Singlet†	Anion radical‡
DMS	0.16 ± 0.02	0.042 ± 0.005	–
dT_6-St-dA_6	0.38 ± 0.04	2.0 ± 0.4 (2.2 ± 0.1)	–
4GC	0.35 ± 0.04	1.4 ± 0.2 (1.8 ± 0.1)	>10
3GC	0.26 ± 0.03	1.0 ± 0.2 (1.4 ± 0.1)	>10
2GC	0.14 ± 0.02	0.29 ± 0.03 (0.5 ± 0.1)	4.0 ± 1
1GC	0.04 ± 0.01	0.005 ± 0.001	0.14 ± 0.01
0GC	<0.01	0.001 ± 0.0002	0.026 ± 0.003
DAS	<0.01	–	0.73 ± 0.05

*Fluorescence quantum yields Φ_f were determined with 330-nm excitation by the use of phenanthrene as an actinometer [$\Phi_f = 0.13$ in cyclohexane; see (*22*)]. †Singlet-state decay times were determined from transient absorption data or fluorescence decays (values in parentheses). ‡Anion radical decay times were determined from transient absorption data.

REFERENCES AND NOTES

1. E. K. Wilson, *Chem. Eng. News* 33 (24 February 1997); G. Taubes, *Science* **275**, 1420 (1997); D. N. Beratan, S. Priyadarshy, S. M. Risser, *Chem. Biol.* **4**, 3 (1997).
2. M. R. Arkin *et al.*, *Science* **273**, 475 (1996).
3. C. J. Murphy *et al.*, *ibid.* **262**, 1025 (1993).
4. D. B. Hall, R. E. Holmlin, J. K. Barton, *Nature* **382**, 731 (1996).
5. P. J. Dandliker, R. E. Holmlin, J. K. Barton, *Science* **275**, 1465 (1997).
6. A. M. Brun and A. Harriman, *J. Am. Chem. Soc.* **114**, 3656 (1992).
7. E. J. C. Olson, D. Hu, A. Hörmann, P. F. Barbara, *J. Phys. Chem. B* **101**, 299 (1997).
8. P. Lincoln, E. Tuite, B. Nordén, *J. Am. Chem. Soc.* **119**, 1454 (1997).
9. S. Priyadarshy, S. M. Risser, D. N. Beratan, *J. Phys. Chem.* **100**, 17678 (1996).
10. R. L. Letsinger and T. Wu, *J. Am. Chem. Soc.* **117**, 7323 (1995).
11. D. H. Waldeck, *Chem. Rev.* **91**, 415 (1991).
12. T. Shida, *Electronic Absorption Spectra of Radical Ions* (Elsevier, Amsterdam, 1988).
13. The hairpin structures were calculated with a modified molecular mechanics (MM2) force field within Hyperchem V5.01 (Hypercube, Waterloo, Ontario).
14. K. M. Guckian *et al.*, *J. Am. Chem. Soc.* **118**, 8182 (1996).
15. F. D. Lewis *et al.*, *ibid.* **117**, 8785 (1995).
16. Fluorescence decays were determined by means of a Photon Technology International Model LS1 photon-counting apparatus with a minimum time resolution of ~0.3 ns.
17. The samples were contained in a 2-mm path length cuvette and had absorbances of about 0.1 at 340 nm. An amplified Ti-sapphire–based laser system was used to pump an optical parametric amplifier to generate ~300-fs, 680-nm pulses (frequency doubled with a potassium dihydrogen phosphate crystal to obtain 340-nm pulses) at a 1.36-kHz repetition rate. Samples were excited with 100 nJ of 340-nm light focused to a 250-μm spot. Absolute transient absorption changes were on the order of 0.01. The uncertainty of the kinetic data increases in the nanosecond regime. For a description of the laser system, see S. R. Greenfield, W. A. Svec, D. Gosztola, M. R. Wasielewski, *J. Am. Chem. Soc.* **118**, 6767 (1996); S. R. Greenfield and M. R. Wasielewski, *Opt. Lett.* **20**, 1394 (1995).
18. The stilbenedicarboxamide singlet state reduction potential is estimated to be ~1.5 V from the sum of its singlet energy (3.4 V) and reduction potential in dimethyl sulfoxide solution [−1.9 V versus standard calomel electrode (SCE)] (*15*). The oxidation potential of dimethylaniline is 0.78 V versus SCE [D. Rehm and A. Weller, *Isr. J. Chem.* **8**, 259 (1970)].
19. N. Mataga, S. Nishikawa, T. Asahi, T. Okada, *J. Phys. Chem.* **94**, 1443 (1990).
20. S. Steenken and S. V. Jovanovic, *J. Am. Chem. Soc.* **119**, 617 (1997).
21. L. P. Candeias and S. Steenken, *ibid.* **111**, 1094 (1989).
22. J. B. Birks, *Photophysics of Aromatic Molecules* (Wiley-Interscience, London, 1970), p. 128.
23. Supported by the Division of Chemical Sciences, Office of Basic Energy Sciences, U. S. Department of Energy, under contracts DE-FG02-96ER14604 (to F.D.L.) and W-31-109-ENG-38 (to M.R.W.). We thank J.-S. Yang for the measurement of fluorescence decays.

7 April 1997; accepted 5 June 1997

Evidence for Interacting Gas Flows and an Extended Volatile Source Distribution in the Coma of Comet C/1996 B2 (Hyakutake)

Walter M. Harris,* Michael R. Combi, R. Kent Honeycutt,
Béatrice E. A. Mueller, Frank Scherb

Images of comet C/1996 B2 (Hyakutake) taken during its close approach to Earth show differences in the distribution of gas and dust in the inner coma and reveal two arc-shaped molecular resonant emission features. The morphology of these features, as well as the apparent decoupling gas from dust in the inner coma, suggest that an extended region of icy grains surrounds the nucleus of Hyakutake and contributes substantially to the production of volatiles. Model simulations suggest the same conclusion and indicate that the brighter arc is explainable by the presence of a trailing condensation of ice-bearing granules with a rate of volatile production approximately 23 percent of that of the nucleus.

The approach of comet C/1996 B2 (Hyakutake) to within 0.102 astronomical units (AU) (*1*) of Earth provided ground-based observers with an opportunity to monitor the characteristics of the extreme inner coma of an active comet. Such close encounters with comets are relatively rare, and recent opportunities to study small-scale (≤100 km) structures near comet nuclei have been limited except for the IRAS-Araki-Alcock (C/1983d) apparition and the Giotto and Vega fly-by encounters with 1P/Halley in 1986 (*2*–*4*). We report on the results of observations performed at the 3.5-m WIYN (*5*) telescope on 26 March 1996, using narrow-band filters (*6*) to image the structure and evolution of different small-scale gas and dust structures within 3.5 arc min (~16,000 km) of Hyakutake's nucleus over 7 hours. These images reveal differences in the radial intensity fall-off and the relative spherical distributions of gas and dust emissions in the inner coma, and show a pair of low-contrast arc-shaped emission features located antisunward of the nucleus (Fig. 1).

Hyakutake was 0.107 AU (*1*) from Earth on 26 March, and this corresponds to 77 km/arc sec, or 15.4 km/pixel in our images. Observations occurred between 5:15 to 12:45 universal time (UT), which was slightly longer than the 6-hour, 14-min rotation period of the nucleus (*7*). We alternated imaging sequences between two filters that isolated either dust at 4850 Å (*6*) or resonant emission of the $[B^2\Sigma^+ - X^2\Sigma^+, \Delta\nu = 0]$ CN band between 3845 and 3883 Å (*8*). The continuum and CN images were taken 360 s apart to facilitate subtraction of dust emission in the CN filter bandpass. The CN and continuum sequences were interrupted at 8:10 UT for an observation of OH $[A^2\Sigma^+ - X^2\Pi_i$, 0-0; 1-1] emission at wavelengths between 3064 and 3115 Å (*8*). After standard processing (*9*), each image was spatially filtered to emphasize small-scale structures, including temporally variable jet features that rotated with the nucleus (*10*). The dust emission present in the CN and OH images was removed by assuming that the jet features in the filtered images contained only dust within 250 km of the nucleus (*11*). The subtraction is then performed using a scaled dust image that removes these jet features.

The surface brightnesses (B_s) of the dust, CN, and OH comae decreased with projected angular distance (ρ) from the nucleus in a manner similar to other comets (*12*). The radial fall-off in the dust coma displayed a typical surface brightness (B_{dust}) dependence of $B_{dust} \sim \rho^{-1}$ consistent with scattering of sunlight from optically thin dust with a number density (N_{dust}) distribution of $N_{dust} \propto r^{-2}$ around the nucleus (Fig. 2A) (*13*). This rate of decreasing intensity was the same for all angles from the sunward direction despite a clear asymmetry in dust production favoring the sunlit hemisphere. Both the CN (Fig. 2B) and OH images displayed radial surface brightness (B_{CN} and B_{OH}) distributions slower than ρ^{-1}, which is consistent with model simulations where these species are created over an extended region by photodissociation of parent molecules drifting away from the nucleus (*14*).

The density of dust in the inner coma was higher in the sunward-facing hemisphere (Fig. 2A), which agreed with the spatially filtered images showing discrete

---

W. M. Harris, Space Astronomy Laboratory, University of Wisconsin, 1150 University Avenue, Madison, WI 53706, USA.
M. R. Combi, Space Physics Research Laboratory, University of Michigan, 2455 Hayward Avenue, Ann Arbor, MI 48109–2143, USA.
R. K. Honeycutt, Department of Astronomy, Indiana University, Swain Hall West, Bloomington, IN 47405, USA.
B. E. A. Mueller, National Optical Astronomy Observatories, 950 North Cherry Avenue, Tucson, AZ 85719, USA.
F. Scherb, Department of Physics, University of Wisconsin, 1150 University Avenue, Madison, WI 53706, USA.

*To whom correspondence should be addressed. E-mail: wharris@sal.wisc.edu